*Int. J. Electrochem. Sci.*, 8 **(2013)** 2918 - 2931

International Journal of
ELECTROCHEMICAL
SCIENCE
www.electrochemsci.org

# $Fe_2O_3$/CNTs Composites as Anode Materials for Lithium-Ion Batteries

*Yifan Sun*[1], *Jingjing Zhang*[1], *Tao Huang*[1], *Zhaolin Liu*[2,*], *Aishui Yu*[1,*]

[1] Department of Chemistry, Shanghai Key Laboratory of Molecular Catalysis and Innovative Materials, Institute of New Energy, Fudan University, 2205 Songhu Road, Shanghai 200433, China
[2] Institute of Materials Research and Engineering, Agency for Science, Technology and Research (A*STAR), 3 Research Link, Singapore 117602, Singapore)
[*]E-mail: asyu@fudan.edu.cn , zl-liu@imre.a-star.edu.sg

*Received:* 19 December 2012 / *Accepted:* 11 January 2013 / *Published:* 1 February 2013

The composites of $Fe_2O_3$/carbon nanotubes ($Fe_2O_3$/CNTs) were synthesized by ammonia hydrolysis and following pyrolysis. A possible explanation was put forward to explain the key role of the CNTs environments in determining the crystal phase of $Fe_2O_3$ in the hybrid structure. When applied as anode materials in lithium-ion batteries (LIBs), the effect of $Fe_2O_3$/CNTs weight ratio and pyrolysis temperature on the electrochemical performance of $Fe_2O_3$/CNTs composites have been researched. The electrode of M-400 (44.8% $Fe_2O_3$) delivers a charge capacity of 619 mAh $g^{-1}$ after 80 cycles at 50 mA $g^{-1}$ with excellent cyclability (94.9% capacity retention), and retained 376 mAh $g^{-1}$ at the rate of 500 mA $g^{-1}$. Compared with pure CNTs and $Fe_2O_3$, the improved electrochemical performance of $Fe_2O_3$/CNTs composites could be attributed to the combined effects of uniformly dispersed $Fe_2O_3$ nanoparticles, highly strong network as well as facilitation of electron transfer contributed by CNTs.

**Keywords:** Iron oxide; Carbon nanotubes; Anode materials; Lithium-ion batteries;

## 1. INTRODUCTION

With advantages including high specific energy, superior energy density, stable cycling and less memory effect, lithium-ion batteries (LIBs) are becoming the main power source in portable electronic devices [1-3]. Currently, the anode material for commercial LIBs is graphite, a traditional carbonaceous material with low electrical potential with respect to lithium, good electric conductivity and superior safety [4]. However, it is no longer the best candidate for anode material. The low

specific capacity (theoretically 372 mAh $g^{-1}$) and poor rate performance of graphite are still behind the demand of high-level LIBs.

During past few years, research and development both at the level of academia and industry have predominantly targeted performance optimization of prevalent electrode materials as well as synthesis of new materials. Transition-metal oxides (MO, where M is Fe, Co, Ni, Cu, etc.) have attracted more and more attractions because of high theoretical specific capacity due to the conversion mechanism, which is different from the intercalation mechanism of graphite. Among these metal oxides, $Fe_2O_3$ is one of the most ideal materials because of its high specific capacity (theoretically 1007 mA h $g^{-1}$), huge abundance, low cost and environmental benignity [5-10]. Nevertheless, during discharge/charge process, $Fe_2O_3$ suffers from crumbling and pulverization, and consequent disconnection with the current collector usually leads to fast capacity fading [11-13]. Another problem is the severe agglomeration of active materials, which cause the reduction of active surface area [13]. These drawbacks have hindered the extensive practical application of $Fe_2O_3$ in LIBs. So how to fabricate truly stable $Fe_2O_3$ anodes as well as alleviate the agglomeration of $Fe_2O_3$ particles remains a great challenge.

So far, an enormous amount of efforts have been made to circumvent the above issues. Typically, there are two main ways to overcome these shortcomings. One is to synthesize nanostructured $Fe_2O_3$ with various nanoscale morphologies, including nanoparticles [14], nanocubes [15], nanorods [16], nanowires [17] and microspheres [18]. The other is to fabricate hybrid nanostructure, where the active material, $Fe_2O_3$, is embedded into the conductive matrix or coated with coating layers via chemical bonding or noncovalent forces [19-23]. Carbon materials are widely applied as conductive matrix and coatings because of diverse adaptability, unique electronic behaviors which can ensure the electronic transport for $Fe_2O_3$ and high strength for accommodating the strain volume changes during the discharge/charge process [24-27]. In addition to all the desired functions of each constituent, some strong synergetic effect can be achieved by integrating the individual components, hence realizing the full potential of the hybrid structure [28].

Herein, we report a simple method to fabricate $Fe_2O_3$/CNTs composites. The formation of the composites at different $Fe_2O_3$ content and pyrolysis temperatures are investigated. The electrochemical performances of $Fe_2O_3$/CNTs composites are tested as anode materials for LIBs. The results indicate that optimized $Fe_2O_3$/CNTs composites exhibit not only higher capacity, but also superior stability and better rate performance.

## 2. EXPERIMENTAL PART

### *2.1 Materials synthesis*

All the chemicals were analytically pure. Multi-walled carbon nanotubes (MWCNTs) were supplied by TCI Shanghai Co. Ltd. (Shanghai, China). The outer diameters and length of the CNTs

were 20-40 nm and 1-2 μm. CNTs were treated at 100 °C with the mixture of concentrated nitric acid and sulfuric acid ($HNO_3$:$H_2SO_4$ = 3:1, v/v) for 2 h in order to remove the residual catalysts and to functionalize the nanotubes. Then purified CNTs were obtained after cooling down to room temperature, extensively rinsed with distilled water and being dried in vacuum under 60 °C for 12 h.

The $Fe_2O_3$/CNTs composites were prepared by the ammonia-atmosphere pre-hydrolysis post-synthetic route [29]. In a typical experiment, 0.1g purified CNTs were dispersed in 10 wt% ethanolic solution containing 0.2 g, 0.4 g and 0.6 g $Fe(NO_3)_3 \cdot 9H_2O$. The mixture was continuously stirred at 40 °C until ethanol was evaporated. After being dried at 60 °C under vacuum, the powder was put into a small glass tube which was further placed into a polytetrafluoroethylene bottle containing 20 wt% ammonia solution (~15 mL), without direct contact of the powder and the ammonia solution. Then the sealed bottle was heated in an oven at 60 °C for 3 h. After cooling, the product was filtered and washed with distilled water. Then the hydrolyzed product was pyrolyzed at 200-500 °C for 2 h with a heating rate of 10 °C $min^{-1}$ under a constant flow of $N_2$. The final composites were obtained and denoted as X-T, where X (S, M, L) represents the content of $Fe_2O_3$ (%) while T stands for the pyrolysis temperature (°C). Pure $Fe_2O_3$ were also prepared in the same way and pyrolyzed at 400 °C for 2 h without the addition of CNTs.

### *2.2 Characterization*

The crystalline structure and morphology of $Fe_2O_3$/CNTs composites were characterized by wide-angle X-ray diffraction (XRD, Bruker D8 Advance, Cu Kα radiation, λ = 1.5406 Å), Fourier transform infrared spectroscopy (FTIR Spectrometer, Nicolet 6700) and field-emission scanning electron microscopy (FE-SEM, Hitachi S-4800). The content of $Fe_2O_3$ in the composites was calculated by thermogravimetric analysis (TG-DTA, DTG-60H, Shimadz).

Electrochemical measurements were performed using a CR2016-type coin cell. An assembled cell was composed of lithium as the counter electrode and the working electrode consisting of 80% active material, 5% super P carbon black and 15% polyvinylidene fluoride (PVDF) made on cooper foil. Coin-type cells were assembled in an argon-filled glove box (Mikarouna, Superstar 1220/750/900) with 1 M $LiPF_6$ solution in ethylene carbonate/diethyl carbonate (EC:DC = 1:1, v/v) as the electrolyte and Celgard 2300 as the separator. The total mass of the active electrode material is about 2-3 mg and the electrode surface area is 1.54 $cm^2$ (Φ 14mm). The galvanostatic charge-discharge tests were performed on a battery test system (Land CT2001A, Wuhan Jinnuo Electronic Co. Ltd.) at a constant current density of 50 mA $g^{-1}$ in the potential range from 0.01 to 3.0 V.

## 3. RESULTS AND DISCUSSION

As schematically illustrated in Fig. 1, the synthesis starts with the creation of a variety of oxygen-containing functional groups on the sidewalls of MWCNTs. Secondly, $Fe(NO_3)_3 \cdot 9H_2O$ is

added as the precursor and $Fe^{3+}$ ions are captured by oxygenous groups on the walls. Then the precursors are converted into hydroxides by in situ hydrolysis under ammonia atmosphere. A subsequent step of pyrolysis at 200-500 °C leads to the nucleation and growth of $Fe_2O_3$ nanoparticles, and the $Fe_2O_3$/CNTs composites are finally obtained. Different from previous studies, we use ammonia-atmosphere instead of alkaline solution to in situ transform $Fe^{3+}$ ions to $Fe(OH)_3$. Reaction with ammonia in the gas phase may contribute to the homogenous hydrolysis and mitigate the agglomeration of $Fe(OH)_3$ particles. The assumption is further supported by the SEM observation that $Fe_2O_3$ particles in the $Fe_2O_3$/CNTs composites and pure $Fe_2O_3$ are smaller and more homogenous than those prepared through alkaline solution hydrolysis reported before [19].

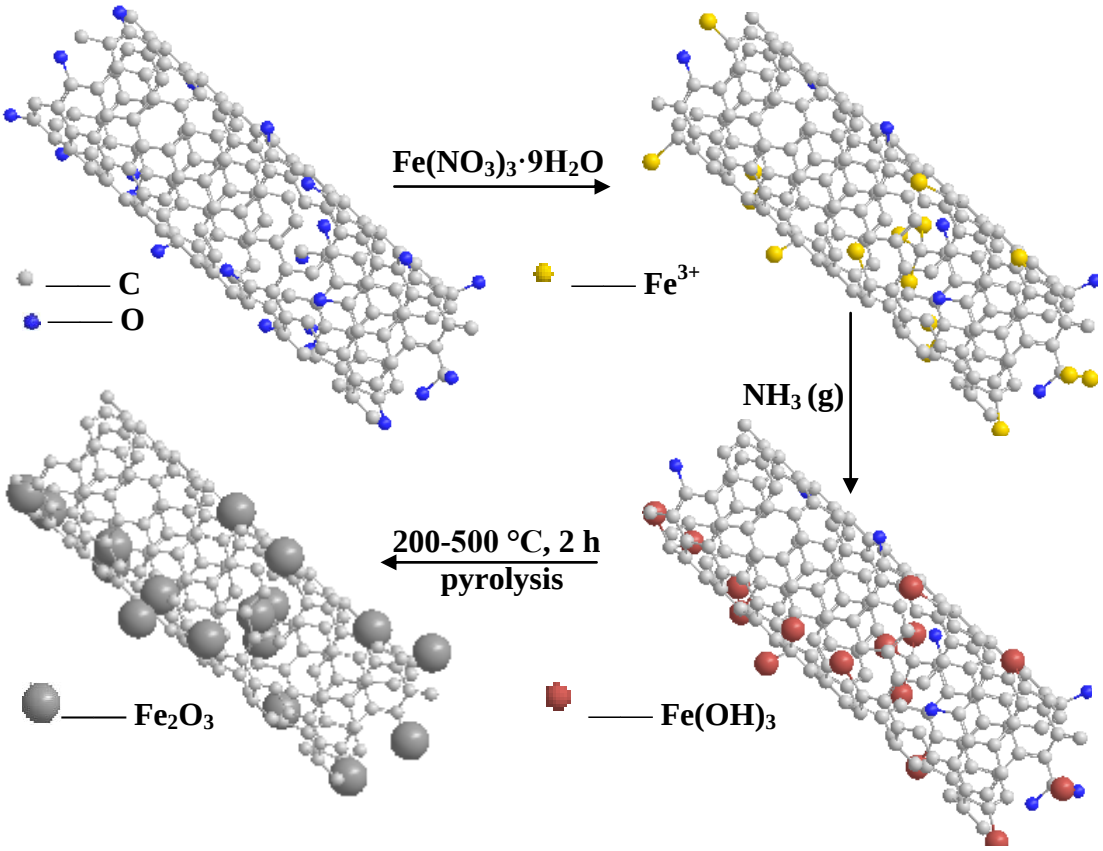


**Figure 1.** A scheme for the synthesis process of $Fe_2O_3$/CNTs composites.

Thermogravimetric analysis results of the composites with different ratios of $Fe_2O_3$/CNTs pyrolyzed at 400 °C are shown in Fig. 2. As can be seen from the curves, the weight loss over the temperature range from 50 to 200 °C is less than 1%, which might be caused by the loss of residual water in the samples [30]. The major weight loss of the composites representing the amount of CNTs

is between 300 and 600 °C. The content of $Fe_2O_3$ in three $Fe_2O_3$/CNTs composites are 28.8%, 44.8% and 55.1%, and the samples are detonated as S-400, M-400 and L-400, respectively.

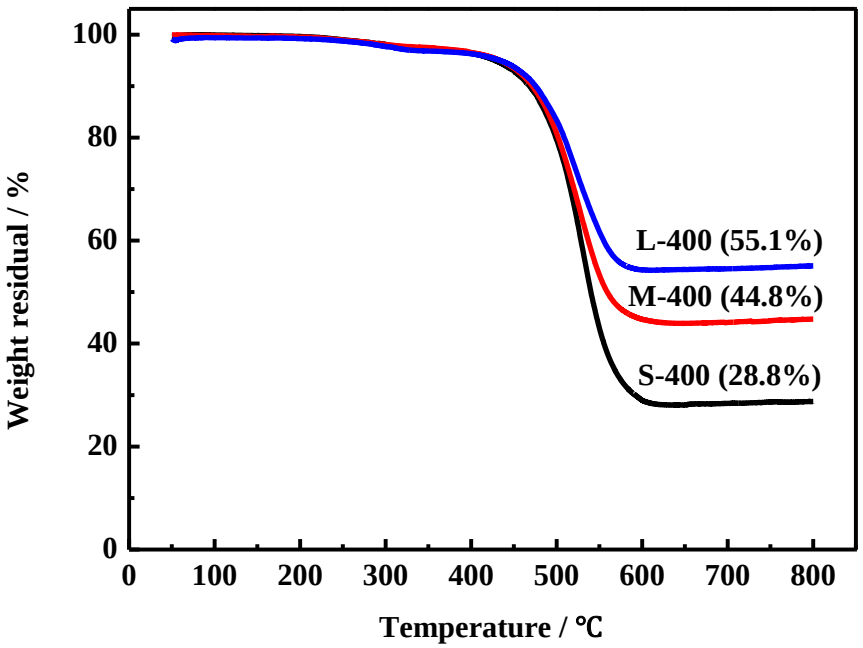


**Figure 2.** Thermogravimetric analysis (TG) curves of S-400 (28.8%), M-400 (44.8%) and L -400 (55.1%).

To investigate the influence of pyrolysis temperature and $Fe_2O_3$/CNTs weight ratio on the formation of $Fe_2O_3$/CNTs composites, XRD diffraction patterns of M-200, M-300, M-400, M-500 and S-400, M-400, L-400 are presented in Fig. 3a and Fig. 3b. The diffraction patterns of pure $Fe_2O_3$ synthesized at 400 °C and purified CNTs are also provided for comparison. Infrared spectrum of S-400 is presented as supporting information.

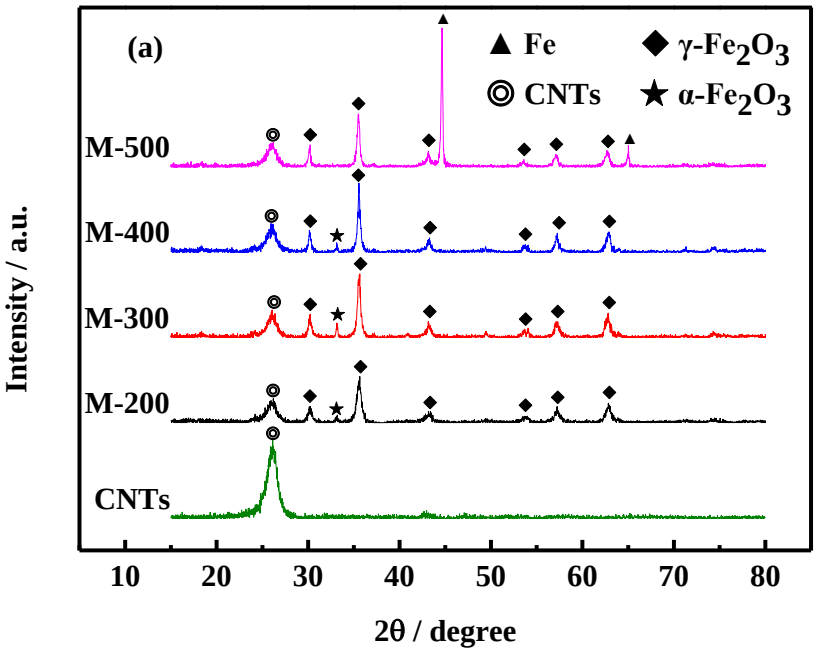

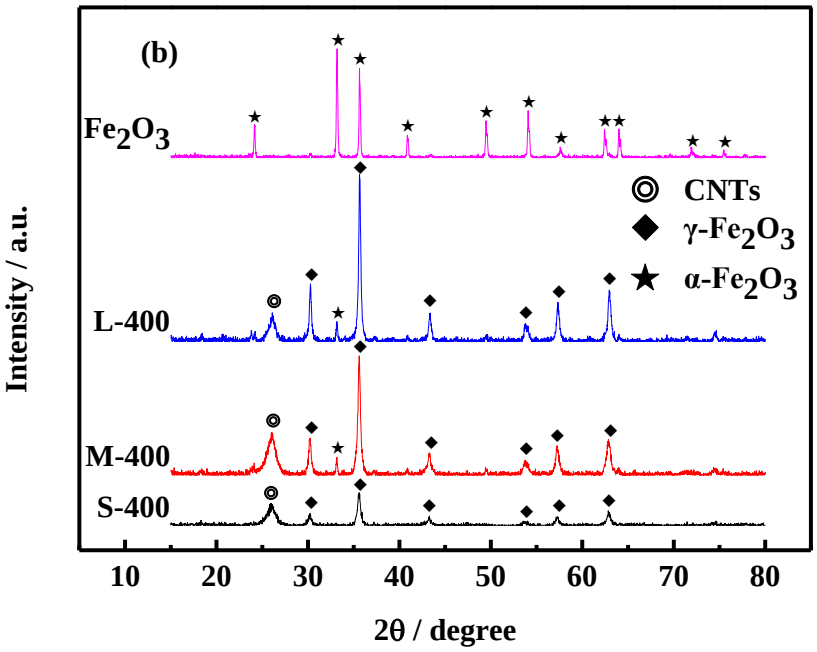


**Figure 3.** Wide-angle XRD patterns of $Fe_2O_3$/CNTs composites, (a) synthesized at different pyrolysis temperatures, (b) at different $Fe_2O_3$ content.

Fig. 3a shows that at the same content of $Fe_2O_3$ (~45%), composites synthesized at 200-400 °C share similar XRD diffraction patterns. Purified CNTs exhibit a distinct peak at 26°, corresponding to the (002) crystal plane of graphite materials. For M-200, M-300 and M-400, the characteristic diffraction peaks at 30.3°, 35.7°, 43.3°, 53.8°, 57.3°, 62.9° and 74.5° match well with the (220), (311), (400), (422), (511), (440) and (533) crystal planes of maghemite (γ-$Fe_2O_3$) (JCPDS No. 89-5892), while the single peak at 33.1° is attributed to the (104) crystal face of hematite (α-$Fe_2O_3$).

When pyrolysis temperature reaches 500 °C, the emergence of two distinct peaks at 43.6° and 63.4°, matched well with the (110) and (200) planes of iron (JCPDS No. 89-4186), indicate the reduction of $Fe_2O_3$ by carbon. Therefore, $Fe_2O_3$ in the composites synthesized at 200, 300 and 400 °C all belong to the mixed phase of maghemite and hematite, hence implying pyrolysis temperature does not play an important role in determining the crystal phase of the composites. In Fig. 3b, it is clear that the crystal structure is closely related with $Fe_2O_3$ content when the synthesis temperature is located at 400 °C. For S-400, the $Fe_2O_3$ content is low (28.8%), and seven distinct diffractions can be assigned to the plane of (220), (311), (400), (422), (511), (440) and (533) of maghemite (γ-$Fe_2O_3$) besides the characteristic peak of CNTs. Additionally, multipeaks can be observed from the Infrared spectrum of S-400 (Fig. 4), which is characteristic of partially ordered γ-$Fe_2O_3$ [31,32], suggesting $Fe_2O_3$ in S-400 is pure γ-$Fe_2O_3$ instead of $Fe_3O_4$. Interestingly, at higher $Fe_2O_3$ content, M-400 (44.8%) and L-400 (55.1%) display similar diffraction patterns of the mixed phase of maghemite and hematite in Fig. 3a. Moreover, for pure $Fe_2O_3$ synthesized at 400 °C, eleven obvious diffraction peaks can be easily

identified for the (012), (104), (110), (113), (024), (116), (122), (214), (300), (1010) and (220) planes of the pure hexagonal phase α-$Fe_2O_3$ crystalline structure (JCPDS No. 33-0664). In brief, $Fe_2O_3$ in the composites gradually finish the phase transition from pure maghemite to the mixture and finally pure hematite with the scale-up of the $Fe_2O_3$/CNTs ratio.

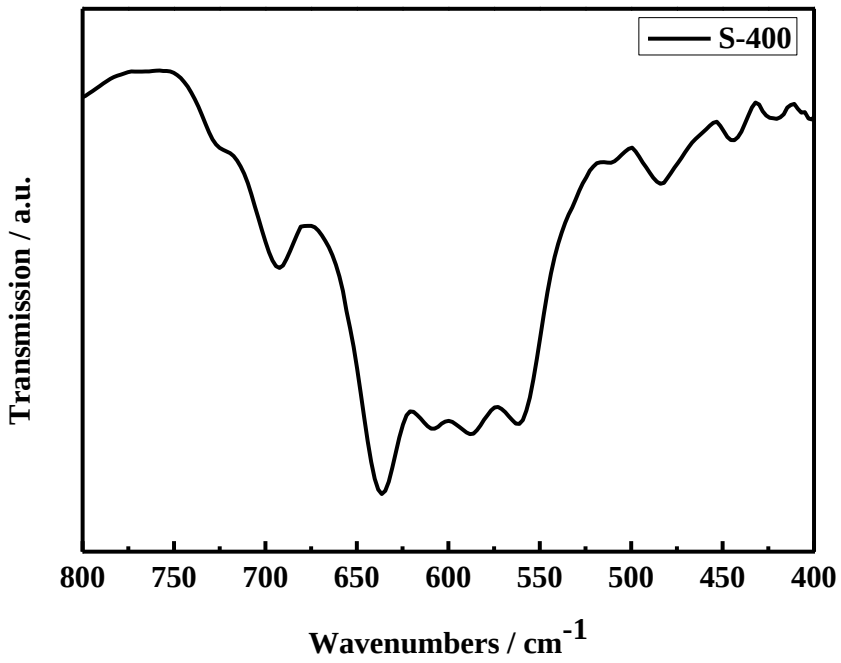


**Figure 4.** Infrared spectrum of S-400.

We conjecture that the phase transition of $Fe_2O_3$ in the composites can be explained by different environments around $Fe_2O_3$ nanoparticles according to various $Fe_2O_3$/CNTs ratios. The low $Fe_2O_3$ content of S-400 indicates that nearly all the $Fe^{3+}$ ions in the precursor can be captured by limited oxygenous groups of CNTs. Consequently, pure phase of $Fe_2O_3$ is expected due to the same reaction environment during hydrolysis and pyrolysis. As the amount of the precursor increases, the functional groups only capture the majority of $Fe^{3+}$ ions and the rest are independent of CNTs. So there are two different environments for the growth of $Fe_2O_3$ particles, one is dependent on CNTs while the other is not. Since the important function of CNTs determining structures of metal oxides have been explained [33], it is reasonable that the dependent ones become maghemite and the independent ones form hematite, leading to the mixed crystal phase.

Fig. 5 shows SEM images of CNTs, α-$Fe_2O_3$, and $Fe_2O_3$/CNTs composites M-400 and L-400. Fig. 5a shows the individual CNT has a smooth surface, typical tube morphology with outer diameter in the range of 20-40 nm. CNTs randomly align to form a network structure, which is beneficial for accommodating the volume expansion and facilitating the transfer of electrons. As can be observed in Fig. 5b, plenty of $Fe_2O_3$ particles are uniformly embedded on the surface of CNTs, roughening the tube

surface. When the content of $Fe_2O_3$ increased, a significant difference could be found between M-400 and L-400 (Fig. 5c), for instance, $Fe_2O_3$ particles are less uniformly dispersed in the network structure and minor aggregation outside CNTs can be observed. As displayed in Fig. 5d, pure α-$Fe_2O_3$ particles are aggregated by many small ones with a size distribution of 100-400 nm. The coral-like bulk α-$Fe_2O_3$ particles are much larger than those in the composites, suggesting that CNTs may effectively impede the aggregation of the $Fe_2O_3$ particles.

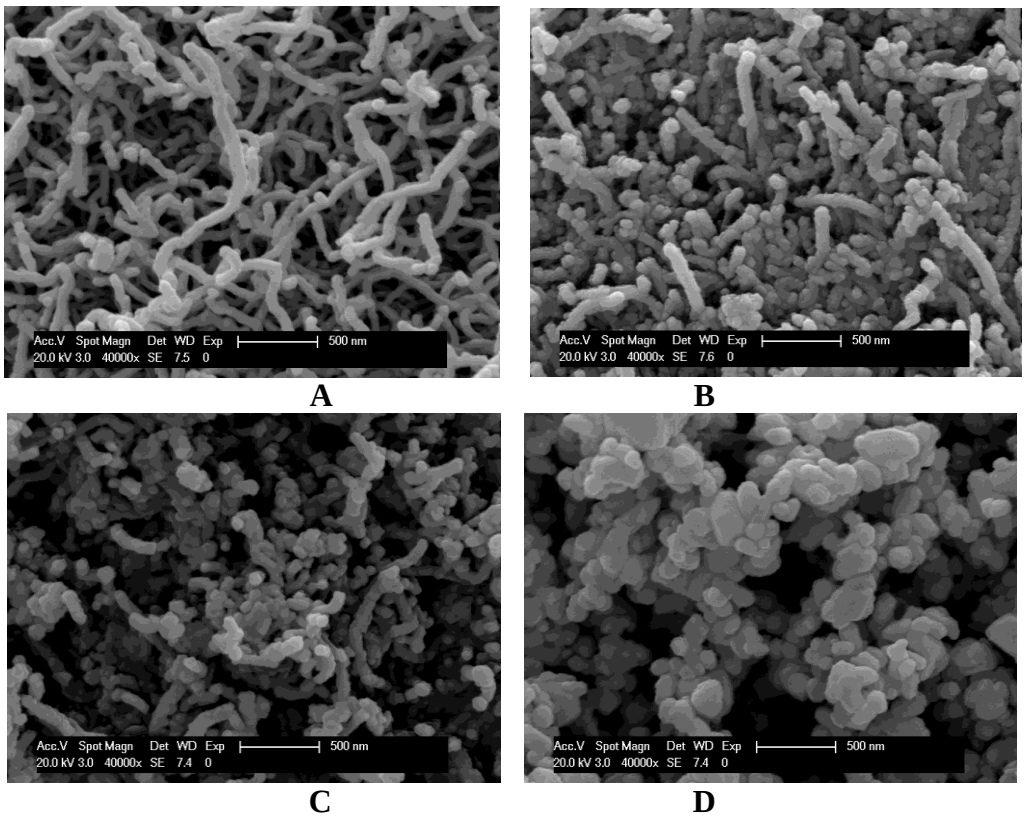


**Figure 5.** SEM images of (a) CNTs, (b) M-400, (c) L-400, (d) $Fe_2O_3$.

To investigate the electrochemical properties of the $Fe_2O_3$/CNTs composites as anode materials in rechargeable LIBs, charge-discharge test was carried out using coin-type cells with a voltage cutoff of 3.0-0.01 V and a current density of 50 mA $g^{-1}$. Fig. 6a provides capacity profiles of the four composites synthesized at 200-500 °C. M-200 and M-300 possess charge capacities of over 600 mAh $g^{-1}$ during the first few cycles, but slowly fade and reach 554 mAh $g^{-1}$ and 542 mAh $g^{-1}$ after 50 cycles. M-400 is more stable compared with the composites synthesized at lower temperatures, retaining 631 mAh $g^{-1}$ after 50 cycles. For higher temperature, M-500 also shows good stability but owns a poor capacity (392 mAh $g^{-1}$ after 50 cycles) mainly because of the existence of the inactive substance, iron.

Hence 400 °C is the optimized temperature of heat treatment. Higher temperature may contribute to the growth of better crystallinity, which is beneficial for electrochemical performance.

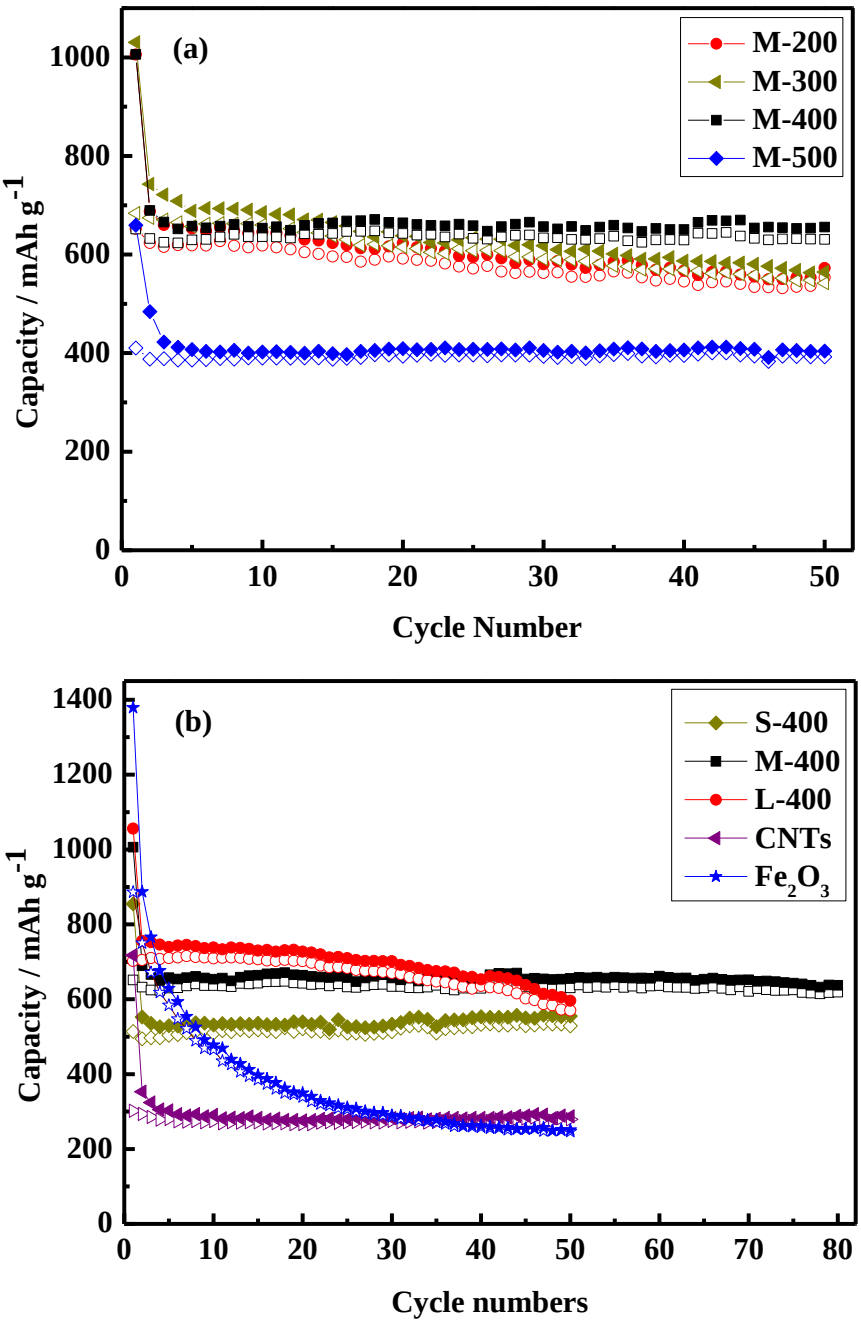


**Figure 6.** The cycling performances of $Fe_2O_3$/CNTs composites, (a) synthesized at different pyrolysis temperatures, (b) at different $Fe_2O_3$ content.

Cyclic performance of the $Fe_2O_3$/CNTs composites at different $Fe_2O_3$ content is also compared with that of purified CNTs and pure $Fe_2O_3$ in Fig. 6b. Purified CNTs show capacity decrease in the

first few cycles, which could be explained by structure re-organization of carbon [34], but then remains stable and retains a charge capacity of 279 mAh $g^{-1}$ after 50 cycles. For pure $Fe_2O_3$, the reversible capacity decreases rapidly and reaches 246 mAh $g^{-1}$ after 50 cycles, 17.8% of its initial value. Obviously, the hybrid structure including S-400, M-400 and L-400 exhibits much better cycling stability than pure $Fe_2O_3$.

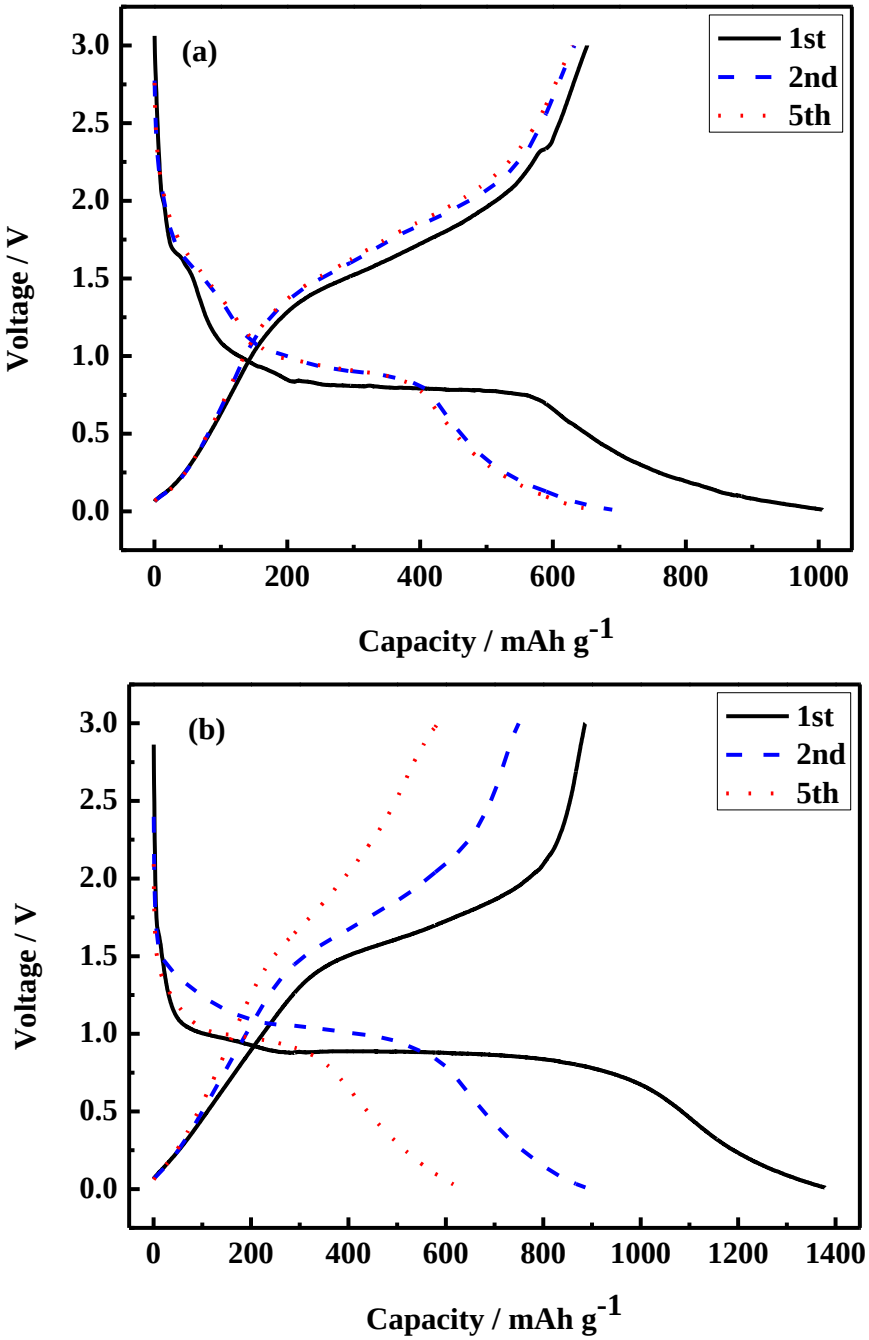


**Figure 7.** The discharge/charge profiles of (a) M-400, and (b) pure $Fe_2O_3$ at the 1st, 2nd and 5th cycle.

With the increase of $Fe_2O_3$ content in the $Fe_2O_3$/CNTs composites, capacities of the electrodes rise correspondingly, but at the cost of sustainable cyclic performance. The charge capacities of S-400, M-400 and L-500 electrodes after 50 cycles are 529, 631 and 570 mAh $g^{-1}$, corresponding to 102.9%, 96.8% and 81.2% of the initial values. It is worth mentioning that after 80 cycles, M-400 electrode exhibits a charge capacity of 619 mAh $g^{-1}$ as 94.9% of the initial value, which shows superiority over previous works [19,35]. Compared with pure $Fe_2O_3$, pronounced enhancement of stability of S-400 and M-400 is attributed to the dispersion of $Fe_2O_3$ particles in the hybrid structure, restrain of volume expansion and improved conductivity all with the assistance of CNTs. By contrast, the inferior cyclability for L-400 is risen from less uniformly dispersion caused by the excess of $Fe_2O_3$, and consequent agglomerations of the independent $Fe_2O_3$ particles result in the relapse of $Fe_2O_3$.

Fig. 7 depicts more details about the voltage profiles of M-400 and pure $Fe_2O_3$ at a current density of 50 mA $g^{-1}$ in the voltage window of 0.01–3.0 V (vs. $Li/Li^+$). As observed in Fig. 7a, the first discharge capacity of M-400 is as high as 1006 mAh $g^{-1}$. When fully discharged, 64.8% (652 mA h $g^{-1}$) of the stored lithium can be extracted upon charging to 3.0 V. The poor coulombic efficiency of the first cycle is a result of the high irreversible capacity during the first discharge process, which is typical for nanostructured active materials with large electrode/electrolyte contact areas.

Accordingly, the charge capacity decreases slightly to 633 and 630 mAh $g^{-1}$ at the 2nd and 5th cycle. Pure $Fe_2O_3$ (Fig. 7b) delivers the initial discharge and charge capacities of 1379 and 886 mA h $g^{-1}$, corresponding to a coulmobic efficiency of 64.3%. However, the charge capacity fades quickly and retains 750 and 584 mAh $g^{-1}$ at the 2nd and 5th cycle. It is noted that the initial discharge capacity of pure $Fe_2O_3$ is even higher than the theoretical capacity of $Fe_2O_3$. This phenomenon has been widely reported for transition metal oxides, usually ascribed to the formation of the SEI film and possibly interfacial lithium storage [36].

As displayed in Fig. 7a and Fig. 7b, in the first discharge curve, two small potential plateaus at around 1.6 and 1.1 V as well as an obvious one at 0.85 V are observed, indicating the following lithiation process containing three steps in sequence [37].

$$Fe_2O_3 + x\ Li^+ + x\ e^- \longrightarrow Li_xFe_2O_3$$

$$Li_xFe_2O_3 + (2-x)\ Li^+ + (2-x)\ e^- \longrightarrow Li_2Fe_2O_3$$

$$Li_2Fe_2O_3 + 4\ Li^+ + 4\ e^- \longleftrightarrow 2\ Fe^0 + 3\ Li_2O$$

In the first charge curve, an extended gradient plateau in the range of 1.5-2.2 V is an indication of the oxidation reactions from $Fe^0$ to $Fe^{3+}$.

The rate capabilities of $Fe_2O_3$/CNTs composites, CNTs and $Fe_2O_3$ are compared at the current of 50 mA $g^{-1}$, 100 mA $g^{-1}$, 200 mA $g^{-1}$ and 500 mA $g^{-1}$ for 10 cycles each in Fig. 8. The charge capacity of $Fe_2O_3$ drops markedly at 500 mA $g^{-1}$ and finally arrives at 187 mA h $g^{-1}$. Three

$Fe_2O_3$/CNTs composites all exhibit improved rate capabilities, presenting charge capacities of 323, 377 and 404 mAh $g^{-1}$ at 500 mA $g^{-1}$. It is noted that nearly the same capacity can be regained for the composites when the current density is turned back to 50 mA $g^{-1}$, indicating superior stability of the composites. The enhanced rate capabilities of $Fe_2O_3$/CNTs composites are resulted from the network structure provided by CNTs, not only favors electron transportation, but also limits volume expansion during cycling.

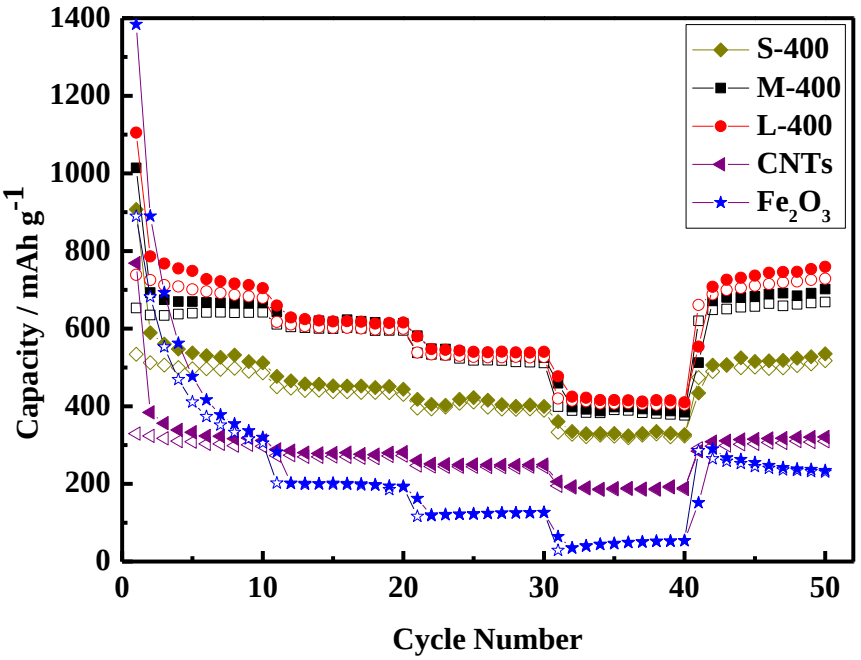


**Figure 8.** The rate performances of S-400, M-400, L-400, pure $Fe_2O_3$ and CNTs.

## 4. CONCLUSIONS

In summary, the $Fe_2O_3$/CNTs composites have been synthesized by ammonia hydrolysis and subsequent pyrolysis. The factors causing various conditions of crystal phase of $Fe_2O_3$ in the composites have been explored. When used as anode materials for LIBs, the electrochemical performance of $Fe_2O_3$/CNTs composites is much better than that of pure materials and strongly affected by the $Fe_2O_3$/CNTs weight ratio and pyrolysis temperature. Raising the content of $Fe_2O_3$ in the composites led to the increase of the specific capacity, but at the cost of cyclic stability. Our study indicates that the optimized composites (M-400) present the best electrochemical property, exhibiting a charge capacity of 619 mAh $g^{-1}$ after 80 cycles (94.9% capacity retention). The pronounced improvements are associated with the combined effects of highly dispersed $Fe_2O_3$ nanoparticles, strong hybrid structure and better electron transportation originated from CNTs. This work can provide some

instructions to optimize the hybrid structure of iron oxides and carbon matrix for better physicochemical properties.

ACKNOWLEDGEMENTS
The authors acknowledge funding supports from the National Key Basic Research Program of China (973 Program, 2013CB934103), the National Natural Science Foundation (No. 21173054) and Science & Technology Commission of Shanghai Municipality (No. 08DZ2270500), China.

**References**

1. M. Armand, J. M. Tarascon, *Nature* 451 (2008) 652.
2. P. G. Bruce, B. Scrosati, J. M. Tarascon, *Angew. Chem. Int. Ed*. 47 (2008) 2930.
3. B. J. Landi, M. J. Ganter, C. D. Cress, R. A. Dileo, R. P. Raffaelle, *Energy Environ. Sci*. 2 (2009) 638.
4. J. O. Besenhard (Ed.), Handbook of Battery Materials, Wiley-VCH, New York, 1999 (Chapter 4).
5. D. Larcher, D. Bonnin, R. Cortes, I. Rivals, L. Personnaz, J. M. Tarascon, *J. Electrochem. Soc*. 150 (2003) A1643.
6. F. Jiao, J. L. Bao, P. G. Bruce, *Electrochem. Solid-State Lett*. 10 (2007) A264.
7. M. V. Reddy, T. Yu, C. H. Sow, Z. X. Shen, C. T. Lim, G. V. Subba Rao, B. V. R. Chowdari, *Adv. Funct. Mater*. 17 (2007) 2792.
8. C. Z. Wu, P. Yin, X. Zhu, C. Z. OuYang, Y. Xie, *J. Phys. Chem*. B 110 (2006) 17806.
9. H. Liu, G. Wang, J. Park, J. Wang, H. Liu, C. Zhang, *Electrochim. Acta* 54 (2009) 1733.
10. Z. C. Wu, K. Yu, S. D. Zhang, Y. Xie, *J. Phys. Chem*. C 112 (2008) 11307.
11. C. M. Ban, Z. C. Wu, D. T. Gillaspie, L. Chen, Y. F. Yan, J. L. Blackburn, A. C. Dillon, *Adv. Mater*. 22 (2010) E145.
12. G. M. Zhou, D. W. Wang, F. Li, L. L. Zhang, N. Li, Z. S. Wu, L. Wen, G. Q. Lu, H. M. Cheng, *Chem. Mater*. 22 (2010) 5306.
13. J. Z. Wang, C. Zhong, D. Wexler, N. H. Idlris, Z. X. Wang, L. Q. Chen, H. K. Liu, *Chem. Eur. J*. 17 (2011) 661.
14. W. T. Dong, C. S. Zhu, *J. Mater. Chem*. 12 (2002) 1676.
15. P. R. Patil, S. S. Joshi, *Synth. React. Inorg. Met. Org. Chem*. 37 (2007) 425.
16. X. Wang, X. Y. Chen, L. S. Gao, H. G. Zheng, M. R. Ji, C. M. Tang, T. Shen, Z. D. Zhang, *J. Mater. Chem*. 14 (2004) 905.
17. L. C. Hsu, Y. Y. Li, C. Y. Hsiao, *Nanoscale Res. Lett*. 3 (2008) 330.
18. J. J. Zhang, Y. F. Sun, Y. Yao, T. Huang, A. S. Yu, *J. Power Sources* 222 (2013) 59.
19. J. Shao, J. X. Zhang, J. J. Jiang, G. M. Zhou, M. Z. Qu, *Electrochim. Acta* 56 (2011) 7005.
20. S. L. Chou, J. Z. Wang, D. Wexler, K. Konstantinov, C. Zhong, H. K. Liu, S. X. Dou, *J. Mater. Chem*. 20 (2010) 2092.
21. W. J. Yu, P. X. Hou, L. L. Zhang, F. Li, C. Liu, H. M. Cheng, *Chem. Commun*. 46 (2010) 8576.
22. G. Wang, T. Liu, Y. J. Luo, Y. Zhao, Z. Y. Ren, J. B. Bai, H. Wang, *J. Alloys Compd*. 509 (2011) 1216.
23. Y. Ma, G. Ji, J. Y. Lee, *J. Mater. Chem*. 21 (2011) 13009.
24. M. Noh, Y. Kwon, H. Lee, J. Cho, Y. Kim, M. G. Kim, *Chem. Mater*. 17 (2005) 1926.
25. Y. Wang, H. C. Zeng, J. Y. Lee, *Adv. Mater*. 18 (2006) 645.

26. Q. Cao, H. P. Zhang, G. J. Wang, Q. Xia, Y. P. Wu, H. Q. Wu, *Electrochem. Commun*. 9 (2007) 1228.
27. Y. S. Hu, Y. G. Guo, R. Dominko, M. Gaberscek, J. Jamnik, J. Maier, *Adv. Mater*. 19 (2007) 1963.
28. Z. Y. Wang, D. Y. Luan, S. Madhavi, Y. Hu, X. W. Lou, *Energy Environ. Sci*. 5 (2012) 5252.
29. Z. X. Wu, W. Li, P. A. Webley, D. Y. Zhao, *Adv. Mater.* 24 (2012) 485.
30. J. S. Chen, Y. L. Tan, C. M. Li, Y. L. Cheah, D. Luan, S. Madhavi, F. Y. C. Boey, L. A. Archer, X. W. Lou, *J. Am. Chem. Soc*. 132 (2010) 6124.
31. T. J. Daou, J. M. Grenèche, G. Pourroy, S. Buathong, A. Derory, C. Ulhaq-Bouillet, B. Donnio, D. Guillon, S. Begin-Colin, *Chem. Mater.* 20 (2008) 5869.
32. P. Wu, N. Du, H. Zhang, J. X. Yu, D. Yang, *J. Phys. Chem*. C 115 (2011) 3612.
33. W. Q. Han, P. Kohler-Redlich, C. Scheu, F. Ernst, M. Rühle, N. Grobert, M. Terrones, H. W. Kroto, D. R. M. Walton, *Adv. Mater*. 12 (2000) 1356.
34. J. S. Gnanaraj, M. D. Levi, E. Levi, G. Salitra, D. Aurbach, J. E. Fisher, A. Claye, *J. Electrochem. Soc.* 148 (2001) A525.
35. B. T. Hang, T. Doi, S. Okada, J. I. Yamaki, *J. Power Sources* 174 (2007) 493.
36. S. L. Jin, H. G. Deng, D. H. Long, X. J. Liu, L. Zhan, X. Y. Liang, W. M. Qiao , L. C. Ling, *J. Power Sources*, 196 (2011) 3887.
37. D. Larcher, C. Masquelier, D. Bonnin, Y. Chabre, V. Masson, J. B. Leriche, J. M. Tarascon, *J. Electrochem. Soc.* 150 (2003) A133-A139.